RSC Advances

PAPER

View Article Online
View Journal | View Issue

Check for updates

Cite this: *RSC Adv.*, 2026, **16**, 8125

Metal–organic frameworks as effective catalysts for glycerol acetalization: morphology and functionality

Fátima Mirante, [a] Pedro Leo, *[ab] Carlos Palomino, [c] Carlos M. Granadeiro, [a] L. Cunha-Silva [a] and Salete S. Balula *[a]

Glycerol is a major by-product generated in large quantities by the biodiesel industry, and its valorisation is essential to promote the usage of this relatively green energy resource. Conversion into fuel additives as solketal *via* a solvent-free acetalization reaction is one of the most sustainable possible ways to valorise glycerol. The key to the success of this process is the design of an active, selective and robust catalyst. In this work, we investigated how the framework topology and Brønsted acid functionality of different MOF materials can influence their catalytic performance. We selected the microporous UiO-66(Zr) and mesoporous MIL-101(Cr) archetypes and functionalized them with both carboxylic $(-COOH)_2$ and sulfonic $(-SO_3H)$ acid groups. This work reports the first use of acid-functionalized MIL-101(Cr) for the solvent-free production of the fuel additive solketal from glycerol, and the first study to directly compare both MOF families under identical conditions. Reaction parameters were optimized under sustainable, solvent-free conditions. Both UiO-66(Zr)–$(COOH)_2$ and MIL-101(Cr)–SO_3H demonstrated remarkable catalytic activity (>85% conversion and >98% selectivity to solketal after 1 h) and, crucially, maintained exceptional structural stability with no observable loss of activity over ten consecutive catalytic cycles. This study establishes a crucial structure–property relationship, validating both specific MOF functionalities for highly effective and reusable heterogeneous catalysts.

Received 15th October 2025
Accepted 27th January 2026

DOI: 10.1039/d5ra07900d

rsc.li/rsc-advances

Open Access Article. Published on 10 February 2026. Downloaded on 2/16/2026 9:47:31 AM.
This article is licensed under a Creative Commons Attribution-NonCommercial 3.0 Unported Licence.

1. Introduction

The valorization of the substantial amount of crude glycerol formed in the biodiesel industry is imperative.[1] It is well known that biodiesel is a non-toxic, biodegradable and renewable fuel, able to be used to reduce the use of diesel from fossil fuel, promoting a reduction of carbon and particulate matter emissions. Biodiesel has emerged as a promising alternative to fossil fuels, offering a viable route to address pressing environmental concerns. The transesterification of triglycerides, a critical step in biodiesel production, results in the generation of a substantial amount of crude glycerol, accounting for approximately 10% of the total product weight. The resulting excess of crude glycerol in the biorefinery industry necessitates the development of effective valorization strategies to enhance the economic viability and sustainability of biodiesel.[2–4] One of the most promising valorization routes is the acetalization process, where glycerol reacts with carbonyl compounds (such as acetone) to produce cyclic products, primarily solketal (2,2-dimethyl-1,3-dioxolan-4-methanol) and acetal (2,2-dimethyl-1,3-dioxan-5-ol) molecules and water. Solketal is a high-value, bio-based fuel additive with favorable physicochemical properties, making it an environmentally benign substitute for traditional oxygenates like methyl *tert*-butyl ether (MTBE). MTBE has been employed by refiners as the most economical oxygenate additive, with the objective of reducing the production cost of reformulated gasoline. It is also a bio-based product that has demonstrated much lower environmental toxicity than the aforementioned common fuel additives.[5]

The glycerol acetalization reaction is a process that occurs without the use of solvents and is catalyzed by heterogeneous catalysts in either batch or continuous processes.[6,7] The reaction utilizes acid catalysts, such as Amberlyst, mixed oxides (niobium–zirconium), polymeric solids, functionalized activated carbons, acidic mesoporous silica, and supported heteropoly acids.[4,8–12] However, the utilization of these catalysts is often constrained due to their suboptimal textural properties or the leaching of active species in the reaction mixture.[13,14] Consequently, there is a need for further development of catalysts that exhibit both high catalytic activity and structural stability under the reaction conditions. In this regard, metal–organic frameworks (MOFs) represent a versatile category of multifunctional materials, engineered to address requirements

[a]*LAQV/REQUIMTE, Department of Chemistry and Biochemistry, Faculty of Sciences, University of Porto, 4169-007 Porto, Portugal*

[b]*Department of Chemical and Environmental Technology, Universidad Rey Juan Carlos, Calle Tulipán s/n, 28933 Móstoles, Spain. E-mail: pedro.leo@urjc.es*

[c]*Department of Chemistry, University of the Balearic Islands, Cra. de Valldemossa, Palma, 07122, Spain*

© 2026 The Author(s). Published by the Royal Society of Chemistry

Open Access Article. Published on 10 February 2026. Downloaded on 2/16/2026 9:47:31 AM. This article is licensed under a Creative Commons Attribution-NonCommercial 3.0 Unported Licence.

across a diverse spectrum of advanced technological applications.[15] MOF materials exhibit a remarkable capacity for catalytic applications, attributable to their unique hybrid nature, tunable pore size, and extensive variety of topological architectures. This attribute, contingent upon the judicious selection of metal ions and ligands, positions them as promising candidates for catalytic applications.[16] The linear geometry and structural rigidity of terephthalic acid and its derivatives, coupled with the versatile coordination chemistry of their carboxylate moieties, have led to their widespread adoption in the construction of MOF architectures.[17] Additionally, the incorporation of various functional groups is possible with MOF materials based on carboxylic ligands,[18,19] which is a fascinating development. These materials can also provide active sites, enabling the design of a range of catalysts with specific characteristics that are unattainable with traditional porous materials.[20] Owing to their exceptional porosity and chemical robustness, alongside the tunability of their metal centers and functional sites, UiO-66 and MIL-101 frameworks have emerged as prominent candidates in the field of heterogeneous catalysis.[21–23] The architecture of UiO-66(Zr) is composed of $Zr_6O_4(OH)_4$ secondary building units, where hexacoordinated zirconium cations are linked *via* μ_3-O bridges. These clusters are interconnected by terephthalate linkers, yielding a framework characterized by an *fcu* topology and the presence of microporous cages.[24] Simultaneously, the crystal structure of MIL-101(Cr) comprises trimeric metal octahedra interconnected through shared oxygen species and terephthalate ligands.[25] A distinctive characteristic of these MIL-101 materials is their mesoporous nature and the generation of cationic CUSs *via* specific thermal treatments, which subsequently function as active sites for catalysis.[26]

The systematic comparison of various types of MOFs (such as UiO-66(Zr) and MIL-101(Cr)) in the solvent-free production of solketal from glycerol can disclose the real role of acid sites and well address the pore structure. Establishing a direct catalyst structure–property correlation is crucial for advancing the rational design of catalytic MOFs. Therefore, this work aims to investigate the influence of framework architecture—specifically contrasting microporous (UiO-66) and mesoporous (MIL-101) topologies—and Brønsted acid functionality (–COOH and $–SO_3H$) on the solvent-free acetalization of glycerol with acetone. The study systematically evaluates the catalytic activity, selectivity, and overall sustainability of the developed heterogeneous catalysts, including rigorous reusability assessments over ten consecutive cycles to identify the optimal material for industrial application.

2. Materials and methods

2.1. Materials

All chemical reagents and solvents were obtained from commercial suppliers and utilized as received, without undergoing additional purification steps: glycerol (99.92%, Fluka), acetone (≥99%, Sigma-Aldrich), methanol (CH_3OH, ≥99.8%, Fisher Scientific U.K.), sodium hydroxide (NaOH, Fisher Chemical), sodium chloride (NaCl, >99.5%, Panreac), zirconium chloride(IV) ($ZrCl_4$, Alfa-Aesar), zirconyl chloride octahydrate ($ZrOCl_2 \cdot 8H_2O$, ≥99%, Merck), 1,2,4,5-benzenetetracarboxylic acid (BDC-$(COOH)_4$, 96%, Merck), hydrochloric acid (HCl, 37%, Scharlau), *N*,*N*′-dimethylformamide (DMF, Carlo Erba), hydrofluoric acid (HF, 40–45% Sigma-Aldrich), *N*,*N*′-dimethylacetamide (DMA, ≥99.5%, Scharlau), ethanol (EtOH, ≥99.8%, Scharlau), tetramethylammonium hydroxide (TMAOH, 10% aqueous solution, Sigma-Aldrich), chromium(III) nitrate nonahydrate ($[Cr(NO_3)_3]\cdot 9H_2O$, 99%, Alfa-Aesar), chromium trioxide (CrO_3, ≥99%, Sigma-Aldrich), 1,2,4-benzenetricarboxylic acid (H_2BDC-COOH, 98%, Sigma-Aldrich), and terephthalic acid (H_2BDC, 98%, Sigma-Aldrich). Monosodium 2-sulfoterephthalic acid (BDC-SO_3Na, >98%) was procured from Tokyo Chemical Industry.

2.2. Synthesis of catalysts

2.2.1 Synthesis of UiO-66(Zr). UiO-66(Zr) was synthesized as described elsewhere.[27] An autoclave was charged with an equimolar mixture of $ZrCl_4$ and H_2BDC in DMF (12 mL), including HCl (37%, 0.32 mL) and H_2O (1.5 mL). Following 30 min of stirring, solvothermal treatment was carried out at 120 °C for 24 h. The resulting solid was recovered by centrifugation, washed two times with DMF and EtOH, and dried under reduced pressure at 60 °C for 12 h.

2.2.2 Synthesis of UiO-66(Zr)–$(COOH)_2$. UiO-66(Zr)–$(COOH)_2$ was synthesized according to the literature.[28] In a Teflon autoclave, zirconium chloride(IV) (1.6 mmol), 1,2,4,5-benzenetetracarboxylic acid (BDC-$(COOH)_4$) (1.7 mmol) and hydrochloric acid (1 mL) were added to deionized H_2O (7 mL) and stirred vigorously for 20 min at room temperature to ensure the total dissolution of the reagents. Then, the solution was warmed at 100 °C for 72 h, and the resultant white particles were isolated by centrifugation and washed thrice with deionized H_2O, to ensure removal of the reagent excess. Finally, the white sample was dried under vacuum at 60 °C.

2.2.3 Synthesis of UiO-66(Zr)–SO_3H. UiO-66(Zr)–SO_3H was synthesized by a solvothermal route following a procedure similar to that previously described.[29] Briefly, UiO-66(Zr)–SO_3H was prepared by mixing $ZrOCl_2 \cdot 8H_2O$ (3.1 mmol) and BDC-SO_3Na (3.1 mmol) in a solution of formic acid (11.7 mL) and DMA (40 mL). After 30 min of stirring, the mixture was transferred to a 100 mL Teflon-lined stainless-steel autoclave and maintained at 150 °C for 24 h. The resulting white precipitate was isolated *via* centrifugation, washed thoroughly with ethanol, and subsequently dried under vacuum.

2.2.4 Synthesis of MIL-101(Cr). Porous MIL-101(Cr) was synthesized by adapting the protocol originally reported by Férey *et al.*[30] A mixture of $[Cr(NO_3)_3]\cdot 9H_2O$ (2 mmol), H_2BDC (2 mmol) and HF (100 μL) in 10 mL of distilled H_2O was stirred for 30 min at room temperature to ensure homogeneity. The resulting suspension was transferred to a Teflon-lined stainless-steel autoclave and heated at 220 °C for 9 h under static conditions. Following a slow cooling process within the oven, the green precipitate was collected by filtration. The crude product underwent a rigorous purification sequence, consisting

© 2026 The Author(s). Published by the Royal Society of Chemistry

Open Access Article. Published on 10 February 2026. Downloaded on 2/16/2026 9:47:31 AM. This article is licensed under a Creative Commons Attribution-NonCommercial 3.0 Unported Licence.

of two successive treatments with DMF and two with ethanol, before being dried under vacuum.

2.2.5 Synthesis of MIL-101(Cr)–$(COOH)_2$. MIL-101(Cr)–$(COOH)_2$ was synthesized following a modified literature procedure.[31] The organic linkers (1.3 mmol total, with an H_2BDC : H_2BDC-COOH molar ratio of 9 : 1) and TMAOH (63 μL, 10% aqueous solution) were dispersed in 20 mL of deionized H_2O and stirred vigorously for 10 min. Subsequently, $Cr(NO_3)_3 \cdot 9H_2O$ (1.3 mmol) was added, and the mixture was stirred for an additional 30 min at room temperature. The resulting suspension was transferred to a Teflon-lined autoclave and maintained at 180 °C for 24 h. The green particles were then isolated by centrifugation and washed five times with deionized water. To ensure activation, the sample was soaked in methanol for 36 h, with the solvent being replenished every 12 h, before finally being dried under vacuum at 100 °C for 5 h.

2.2.6 Synthesis of MIL-101(Cr)–SO_3H. MIL-101(Cr)–SO_3H was prepared *via* a solvothermal route based on a previously reported method.[32] In a typical synthesis, BDC-SO_3Na (12.5 mmol) and CrO_3 (12.5 mmol) were dissolved in 50 mL of deionized water, followed by the dropwise addition of concentrated HCl (0.91 g) under constant stirring. The resulting mixture was transferred to a Teflon-lined autoclave and maintained at 180 °C for 6 days. After the reaction, the product was isolated by filtration and washed thoroughly with water and methanol. To achieve high purity and ensure pore activation, the solid was treated with 50 mL of hot ethanol at 100 °C for 24 h.

2.3. Characterization of the catalysts

The obtained materials were characterized using powder X-ray diffraction (XRD), argon adsorption–desorption isotherms and infrared spectroscopy (FTIR). Powder XRD patterns were obtained at room temperature on a Rigaku Smartlab diffractometer operating with a Cu radiation source ($\lambda = 1.540593$ Å) and in a Bragg–Brentano $\theta/2\theta$ configuration (45 kV, 200 mA). Intensity data were collected by a step-counting method (step 0.01°), in continuous mode, in the $3 \leq 2\theta \leq 60°$ range, and all the representations are shown in arbitrary units of intensity. Fourier-transform infrared (FTIR) spectra were acquired using the attenuated total reflectance (ATR) operation mode of a PerkinElmer FTIR System Spectrum BX spectrometer, and all the representations are shown in arbitrary units of transmittance. Nitrogen adsorption–desorption isotherms at 77 K were measured using a Tristar II (Micromeritics). Samples were previously evacuated *in situ* under high vacuum for 12 h at 423 K. The surface area was calculated using the Brunauer–Emmett–Teller (BET) model.[33] The pore volume was assessed using the Dubinin–Radushkevich equations and also taken at $P/P_0 = 0.95$ as a single-point value. The pore size distribution, as well as pore volume and diameter, were determined from the adsorption branch of the argon isotherm using non-local density functional theory (NLDFT). The best agreement was obtained with the NLDFT equilibrium kernel model, specifically, N_2 at 77 K in cylindrical pores.[34] Catalytic reactions were periodically monitored by GC-FID analysis carried out using a Bruker 430-CC-FID chromatograph. Hydrogen was used as a carrier gas with a 30 mL min^{-1} flow rate, and a Suprawax-280 capillary column (30 m × 0.25 mm i.d.; 0.25 μm film thickness) was used. The strength of the acidity of different materials was calculated using potentiometric titration using 2 mol per dm^3 NaCl as a cation-exchange agent. The six different MOFs were maintained in contact with NaCl solution (1 : 1 ratio) at room temperature for 24 h under stirring. The suspension was separated by filtration. The final solution was titrated with 0.04 M NaOH solution to determine the acid site loading of the two MOF structures with functional groups.[35]

2.4. Catalytic acetalization of glycerol

The catalytic acetalization of glycerol with acetone was conducted under solvent-free conditions using a 5 mL closed borosilicate glass reactor. The vessel, equipped with a magnetic stirrer, was immersed in a thermostatically controlled liquid paraffin bath to ensure precise temperature regulation. Reaction mixtures were prepared using various glycerol-to-acetone molar ratios, specifically 1 : 1.5, 1 : 3, 1 : 6, and 1 : 15. The initial reaction mixture is biphasic due to the limited miscibility of glycerol and acetone. The mixture was left under agitation for 10 min at the chosen temperature (30 °C, 40 °C and 60 °C) to ensure thermal and mechanical homogeneity. Catalysts were introduced at various weight percentages (4, 8, and 20 wt% of metal content relative to the glycerol substrate) to start the acetalization. Quantitative analysis was performed on a Varian CP-3380 gas chromatograph using a Suprawax-280 column (30 m length, 0.25 mm i.d., 0.25 μm film thickness). H_2 served as the carrier gas with the flow rate maintained at 55 cm^3 s^{-1}. The error for each experiment was determined to be equal to or less than 5% of the conversion of glycerol. The products obtained were identified by gas chromatography coupled with mass spectrometry analysis (GC-MS) using a Hewlett-Packard 5890 chromatograph with a Mass Selective Detector MSD series II. Furthermore, ^{1}H NMR analysis using $CDCl_3$ as a solvent was used to identify solketal, the main product. Spectra were collected using a Varian Mercury Plus spectrometer at 400 MHz using trimethyl silane as an internal standard.

3. Results and discussion

3.1. Catalyst characterization

Fig. 1 shows the powder X-ray diffraction patterns of the pure UiO-66(Zr) (a) and MIL-101(Cr) (b) structures, as well as the functionalized materials. High crystallinity was observed in the XRD diffractograms of all the samples, with peaks aligning well with the simulated diffraction data for UiO-66 and MIL-101. This consistency confirms that the materials were prepared with their respective intended structures and high phase purity. Furthermore, the FTIR-ATR spectra of the functionalized derivatives of the UiO-66(Zr) and MIL-101(Cr) materials clearly reveal new vibrational bands compared with the respective pristine MOF materials. These new bands can be attributed to vibrational modes of the $-CO_2H$ or $-SO_3H$, suggesting the successful preparation of the desired derivative materials. The

Open Access Article. Published on 10 February 2026. Downloaded on 2/16/2026 9:47:31 AM.
This article is licensed under a Creative Commons Attribution-NonCommercial 3.0 Unported Licence.

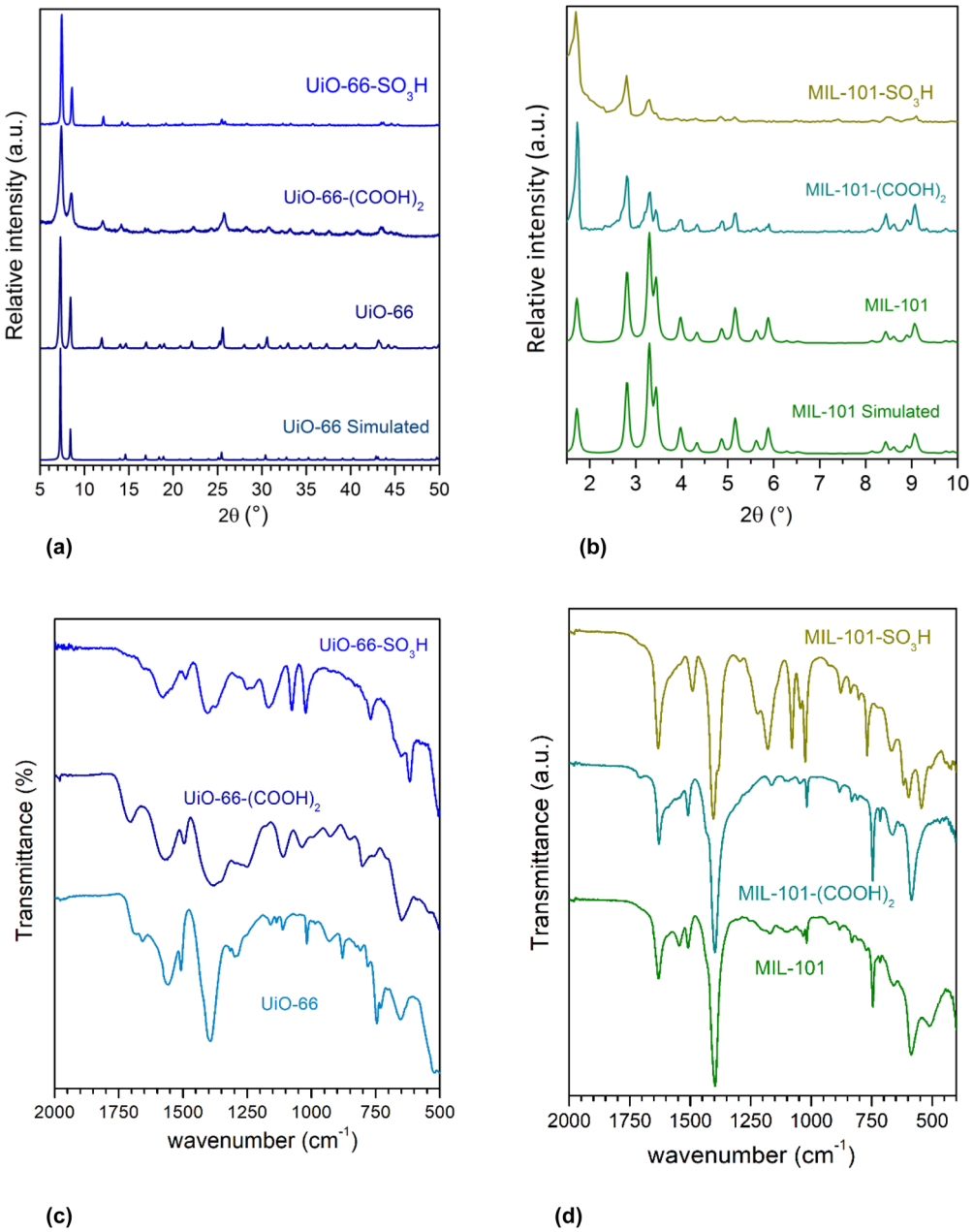

Fig. 1 (a and b) Powder X-ray diffraction patterns of the simulated and experimental UiO-66(Zr) and MIL-101(Cr) materials, respectively. Simulated XRD patterns for UiO-66(Zr) and MIL-101(Cr) were generated from their respective crystallographic data files.[36,40] (c and d) FTIR-ATR spectra of the as-synthesized UiO-66(Zr) and MIL-101(Cr) materials.

experimental evidence of the powder X-ray diffraction and FTIR-ATR spectroscopy is corroborated by the argon adsorption–desorption characterization. Table 1 shows the textural properties of the set of materials evaluated. The N_2 adsorption isotherms (Fig. S1 and S2) and the corresponding pore diameter distributions for all UiO-66 and MIL-101 structures are provided in the SI. The inclusion of the functional groups generally results in lower adsorption and a decrease in surface areas and pore volumes compared to the original structures, which is primarily attributed to the increased framework mass and the steric hindrance imposed by the functional linkers.[36,37] The BET surface area and the total pore volume of UiO-66 functionalized derivatives are significantly reduced. For the pristine UiO-66 and UiO-66-SO_3H material, this reduction is largely due to pore volume occupation, as both exhibit pore diameters centered around 9 Å, and maintain the original *fcu* topology. Crucially, the functionalized UiO-66-$(COOH)_2$ (based on H_4BTEC) is not isostructural with the pristine UiO-66 (H_2BDC). The former adopts an 8-connected *bcu* topology, while the latter is a 12-connected *fcu* framework.[38,39] This inherent difference in topology results in distinct textural parameters and diffusion pathways, which must be considered when interpreting their

© 2026 The Author(s). Published by the Royal Society of Chemistry

Open Access Article. Published on 10 February 2026. Downloaded on 2/16/2026 9:47:31 AM. This article is licensed under a Creative Commons Attribution-NonCommercial 3.0 Unported Licence.

Table 1 Textural properties of the synthesised catalysts

Catalyst	BET[a] ($m^2\ g^{-1}$)	V_p[b] ($cm^3\ g^{-1}$)	D_p (Å)
UiO-66(Zr)	1135	0.68	9
UiO-66(Zr)–$(COOH)_2$	452	0.41	6.5, 12.6
UiO-66(Zr)–SO_3H	390	0.32	9
MIL-101(Cr)	2577	1.44	11, 18, 23
MIL-101(Cr)–$(COOH)_2$	2080	1.27	
MIL-101(Cr)–SO_3H	1506	0.95	

[a] Total surface area calculated by the BET method from the adsorption branch of the corresponding argon isotherm. [b] Total pore volume recorded at $P/P_0 = 0.975$.

catalytic performance, as evidenced by the dual pore distribution (6.5 Å and 12.6 Å) observed for the *bcu* structure.

In contrast, the MIL-101(Cr) structures maintain better textural properties even after functionalization. This stability is attributed to the framework's multimodal pore system (micropores and mesopores) with distinct maxima at 11 Å, 18 Å, and 23 Å. This structural resilience allows the functional groups to be incorporated without causing the significant pore collapse or the dramatic reduction in surface area observed in the UiO-66 derivatives, thereby preserving the efficient accessibility required for the catalytic upgrading of glycerol.

3.2. Acidity characterization

The acidity of the functionalized materials, as well as the pristine materials, was evaluated through potentiometric titration. To quantify exchangeable acidity, the MOFs were suspended in a NaCl solution for 24 h. The pH values, reflecting the exchange of H^+ by Na^+, were subsequently measured and are presented in Table 2. These values suggested that the acid-functionalized MOFs present a higher acidity than the pristine ones. The results in Table 2 suggest that for the UiO-66 family, the carboxylic groups provide a significantly stronger acid site (pH 2.82) compared to the sulfonic groups (pH 4.07). Conversely, for the MIL-101 family, the MIL-101(Cr)–SO_3H material presents the highest acid site loading (0.932 mmol g^{-1}) among all the synthesized materials.

3.3. Catalytic acetalization reaction

The MOFs UiO-66(Zr) and MIL-101(Cr) functionalized with carboxylic and sulfonic groups were tested for the acetalization of glycerol with acetone. The effect of the reaction conditions for glycerol acetalization with acetone was first explored using the UiO-66(Zr)–$(COOH)_2$ as a catalyst. This reaction provides two cyclic products (Scheme 1), *i.e.* the five-membered solketal (**1**) as a principal product and the six-membered acetal (**2**).

Using the UiO-66(Zr)–$(COOH)_2$ heterogeneous catalyst, the glycerol acetalization reaction was optimized by varying different parameters: the temperature, the amount of catalyst and the glycerol : acetone ratio. The initial conditions adopted were 15 mg of catalyst and a 1 : 6 glycerol/acetone ratio.[41] The influence of reaction temperature was studied at 30, 40 and 60 °C, and the results are presented in Fig. 2. We observed that increasing the temperature enhances glycerol conversion after 3 h of reaction. The glycerol conversion demonstrated a similar profile for the three different temperatures during the first 5 min of reaction (32–36%). However, at 15 min of reaction, the higher reaction temperature resulted in a higher glycerol conversion. This is even more noticeable as the reaction time progresses. After 3 h of reaction, the conversion of glycerol was of 87% using 60 °C and 83% for 40 °C. It should be noted that regardless of the reaction temperature used, the selectivity towards solketal is always higher than 98%.

The effect of the amount of catalyst on the acetalization of glycerol was analysed using 15, 30 and 75 mg of catalyst, corresponding to 4, 8 and 20 wt%, respectively. The catalysis

Table 2 pK_a values for the MOFs

MOF	pH (before titration)	Acidity (mmol g^{-1})
UiO-66(Zr)	4.18	0.359
UiO-66(Zr)–$(COOH)_2$	2.82	0.841
UiO-66(Zr)–SO_3H	4.07	0.373
MIL-101(Cr)	4.60	0.134
MIL-101(Cr)–$(COOH)_2$	4.13	0.238
MIL-101(Cr)–SO_3H	3.25	0.932

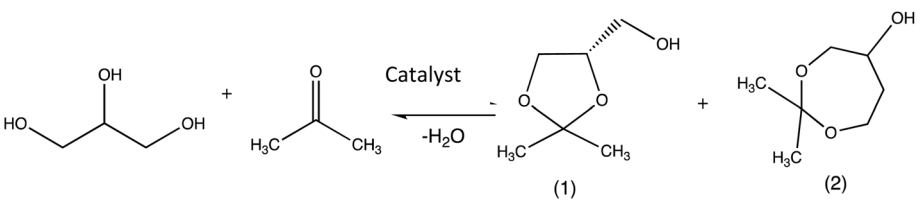

Scheme 1 Glycerol acetalization reaction, where (**1**) corresponds to 2,2-dimethyl-1,3-dioxolan-4-methanol (solketal) and (**2**) 2,2-dimethyl-1,3-dioxan-5-ol (acetal).

Open Access Article. Published on 10 February 2026. Downloaded on 2/16/2026 9:47:31 AM.
This article is licensed under a Creative Commons Attribution-NonCommercial 3.0 Unported Licence.

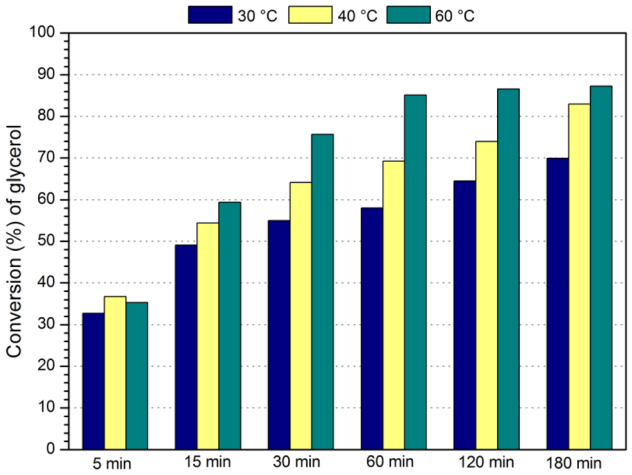

Fig. 2 Conversion for the acetalization of glycerol obtained for UiO-66(Zr)–$(COOH)_2$ using 15 mg (4 wt%) of catalyst, a 1 : 6 glycerol/acetone ratio and different temperatures (30, 40 and 60 °C).

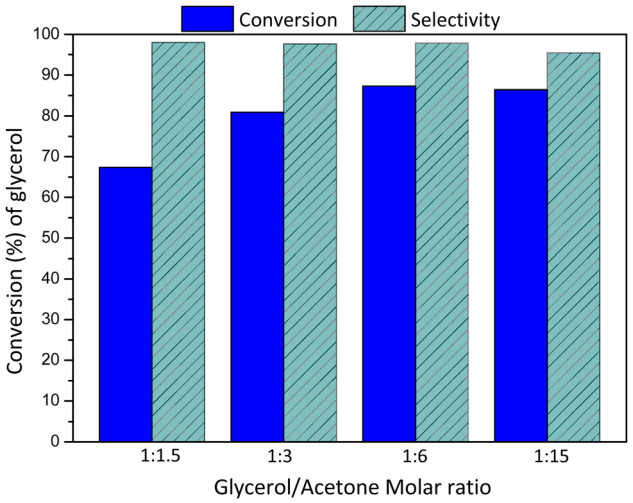

Fig. 4 Conversion for the acetalization reaction and solketal selectivity after 3 h obtained for UiO-66(Zr)–$(COOH)_2$ using 15 mg (4 wt%) of catalyst and different glycerol/acetone ratios at 60 °C.

results are illustrated in Fig. 3. It can be observed that the acetalization reaction profiles for the three catalyst loadings exhibit a similar trend, particularly as they converge after 3 h of reaction. Therefore, in the following studies, the smallest amount of catalyst was used (15 mg, 4 wt%).

To confirm the absence of homogeneous or spurious catalytic effects, a control experiment (blank) was performed under the optimized conditions (60 °C, 1 : 6 glycerol/acetone ratio) but without the addition of a heterogeneous catalyst. The analysis after 3 h showed a glycerol conversion of less than 2%, confirming that the catalytic reaction is exclusively driven by the Brønsted acid sites of the synthesized MOFs and that the reactor system is free from acidic contamination.

The reversible nature of the acetalization reaction necessitates the use of a molar excess of acetone to promote higher conversion by shifting the equilibrium position toward the products.[3,42] To assess this, we studied the effect of the molar ratio of glycerol to acetone from 1 : 1.5 to 1 : 15 (Fig. 4), keeping the other reaction parameters constant (15 mg of catalyst and 60 °C). After 3 h of reaction, an increase in the conversion of glycerol was observed as the molar ratio was changed from 1 : 1.5 to 1 : 6. An effective stabilization of the conversion for glycerol acetalization was observed upon further increasing the excess of acetone beyond a ratio of 1 : 6. This is probably due to the dilution effect.[43] The observed requirement for a stoichiometric excess of acetone and the stabilization of conversion at a 1 : 6 molar ratio is in good agreement with literature reports, confirming the reaction's thermodynamic drive and the need to shift the equilibrium towards the products.[44,45] While increasing the temperature positively influences the initial reaction rate (as observed in Fig. 2), the selection of 60 °C balances kinetics and the known exothermic nature of the acetalization reaction, which otherwise leads to a reduced final equilibrium conversion.[46] Using the optimal ratio of glycerol/acetone of 1 : 6, a solketal yield of 98% was obtained after 3 h of reaction.

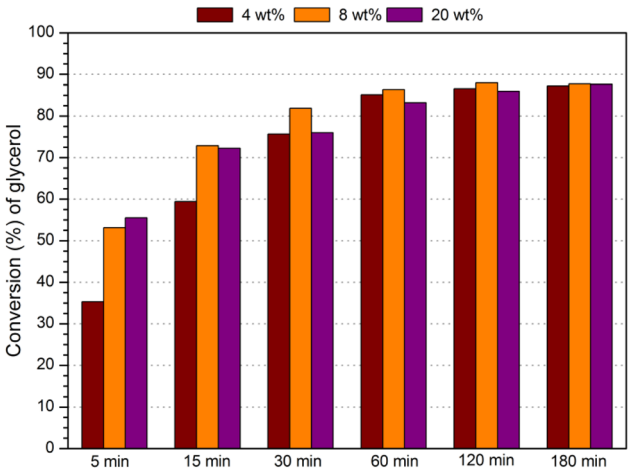

Fig. 3 Conversion for the acetalization of glycerol obtained for different amounts of UiO-66(Zr)–$(COOH)_2$ using a 1 : 6 glycerol/acetone ratio, at 60 °C.

3.4. Comparison of functional groups –$(COOH)_2$ and –SO_3H

Once the optimal reaction conditions were determined, the influences of the functional sulfonic and carboxylic catalytically active groups (–$(COOH)_2$ and –SO_3H) present in the UiO-66(Zr) and MIL-101(Cr) structures were evaluated. All the catalytic MOF samples were activated under vacuum before use in the reaction. This will increase the accessibility of acidic functional groups located in the pores, ensuring the elimination of possible solvent molecules occluded in them. This comparison between structurally distinct frameworks enables a broader understanding of how textural properties and active-site accessibility jointly determine catalytic performance, providing complementary insights that would not be obtained by analyzing only isostructural MOFs.

Considering the results obtained for the acidity of the acid-functionalized MOFs (Table 2), all the reactions were carried

© 2026 The Author(s). Published by the Royal Society of Chemistry

Open Access Article. Published on 10 February 2026. Downloaded on 2/16/2026 9:47:31 AM.
This article is licensed under a Creative Commons Attribution-NonCommercial 3.0 Unported Licence.

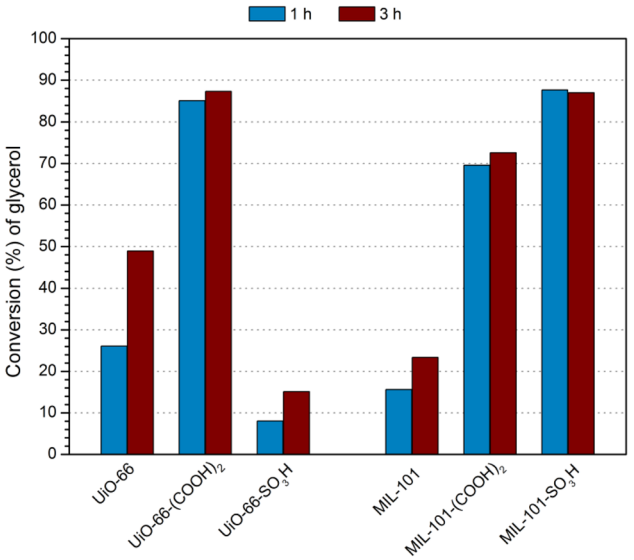

Fig. 5 Conversion data obtained for the acetalization of glycerol after 1 and 3 h, using a 1 : 6 glycerol/acetone ratio at 60 °C.

out with the same concentration of H^+ released by the material UiO-66(Zr)–$(COOH)_2$ (4 wt% of metal in the MOF structure relative to glycerol), adapting the mass of the catalyst to each of the reactions.

Fig. 5 shows the catalytic performance of all materials in terms of the overall glycerol conversion after 1 h and 3 h of reaction time. In view of the results obtained, the presence of active and accessible functional groups allows the catalytic activity of the structures studied to be significantly improved with respect to the original materials, except for the UiO-66(Zr)–SO_3H material, which is the material showing the lowest conversion, which is attributed to the limited accessibility of its acidic sites. Its low pore volume (0.32 $cm^3\ g^{-1}$) likely hinders the diffusion of the viscous glycerol to the active sites, a phenomenon corroborated by the similar acid loading values between UiO-66(Zr)–SO_3H and the pristine UiO-66 (Table 2). The catalytic efficiency of heterogeneous systems is fundamentally linked to their textural properties and internal framework structure.[47] On the other hand, the UiO-66(Zr)–$(COOH)_2$ material presents much higher catalytic activity. In this catalytic MOF, the acidic active centres must be more available for the glycerol acetalization reaction. Therefore, UiO-66(Zr)–$(COOH)_2$ presents slightly better textural properties, and the reaction is favoured using a Brønsted acid catalyst.[4,48] The solketal product obtained after the catalytic reaction using the UiO-66(Zr)–$(COOH)_2$ catalyst with a 1 : 6 glycerol/acetone ratio at 60 °C was characterized by ^1H NMR spectroscopy (Fig. S3). The spectrum confirmed the successful formation of solketal, showing two methyl groups as singlets near 1.35 and 1.40 ppm, along with the characteristic multiple signals around 4.2 ppm corresponding to the –CH and $–CH_2$ protons of the five-membered dioxolane ring (solketal structure).[49]

Conversely, the MIL-101(Cr) structure, characterized by its large mesopores, shows no significant textural limitation for the diffusion of glycerol. The marked difference in activity between MIL-101(Cr)–SO_3H and MIL-101(Cr)–$(COOH)_2$, while maintaining the same nominal H^+ concentration, highlights the importance of the acidic character (strength and loading) in this family. Both functionalized MIL-101 materials significantly outperformed the pristine framework (achieving conversions 3.7 and 3 times higher, respectively), demonstrating that enhancing the intrinsic acidity facilitates glycerol acetalization, provided the active sites are accessible and available within the porous system.

The mechanism of acidic catalytic reaction to form solketal from glycerol and acetone is reasonably well established in the literature.[50–53] Glycerol conversion into solketal over Brønsted acid sites proceeds *via* an initial glycerol–acetone adduct that evolves into a tertiary alcohol. The acid sites on the MOF's SBU promote the dehydration of this species, yielding a reactive carbocation intermediate. Depending on whether the secondary or terminal hydroxyl group of the glycerol backbone performs the intramolecular attack, five- or six-membered rings are produced. The catalytic cycle is completed by the release of a water molecule.

3.4.1 Intrinsic catalytic activity. Given the equilibrium nature of the acetalization reaction, the final conversion values (after 1 and 3 h of reaction) reflect thermodynamic limits. To properly assess the intrinsic catalytic activity of the functionalized MOFs, the turnover frequency (TOF) was calculated at a short reaction time (after 15 min of reaction), where the reaction is kinetically controlled (Table 3). The TOF is based on the H^+ loading determined by potentiometric titration (Table 2).

The MIL-101(Cr)–SO_3H showed the highest intrinsic activity (0.9204 h^{-1}), slightly surpassing the UiO-66(Zr)–$(COOH)_2$ (0.7623 h^{-1}). This result confirms that while the final conversion is similar, the mesoporous structure provides the fastest initial turnover by eliminating diffusion constraints for the viscous glycerol substrate. The superior activity of UiO-66(Zr)–$(COOH)_2$ in the microporous family is, however, remarkable, highlighting the critical role of its stronger Brønsted acidity in accelerating the initial reaction rate, compensating for reduced accessibility.

3.5. Reusability capacity and stability

To address environmental concerns and improve process efficiency, the long-term stability and reuse of the catalyst were investigated over several consecutive catalytic runs. The

Table 3 TOF of the evaluated MOFs. Reaction conditions: 4 wt% of metal in the MOF structure relative to glycerol, using a 1 : 6 glycerol/acetone ratio at 60 °C

MOF	TOF (h^{-1})
UiO-66(Zr)	0.1090
UiO-66(Zr)–$(COOH)_2$	0.7623
UiO-66(Zr)–SO_3H	0.1896
MIL-101(Cr)	0.0911
MIL-101(Cr)–$(COOH)_2$	0.3561
MIL-101(Cr)–SO_3H	0.9204

© 2026 The Author(s). Published by the Royal Society of Chemistry

Open Access Article. Published on 10 February 2026. Downloaded on 2/16/2026 9:47:31 AM.
This article is licensed under a Creative Commons Attribution-NonCommercial 3.0 Unported Licence.

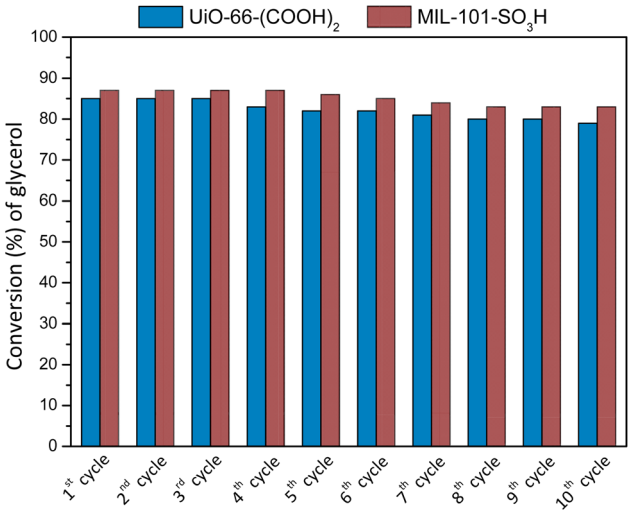

Fig. 6 Conversion results obtained for reuse for ten consecutive glycerol acetalization reactions after 1 h using 15 mg of UiO-66(Zr)–$(COOH)_2$ catalyst or 13.5 mg of MIL-101(Cr)–SO_3H and a 1 : 6 glycerol/acetone ratio at 60 °C.

reusability of the most active catalysts, UiO-66(Zr)–$(COOH)_2$ and MIL-101(Cr)–SO_3H, was investigated over ten consecutive glycerol acetalization reactions. After each reaction, the solution (glycerol and acetone) was removed from the reactor, and the solid catalyst was thoroughly washed with ethanol and dried at 60 °C. This process allowed it to be reused in a subsequent acetalization reaction under identical experimental conditions. Fig. 6 displays the conversion results obtained for the ten consecutive acetalization reactions after 1 h.

It can be observed that the catalysts maintained remarkable performance during all ten consecutive reactions without any significant loss of catalytic efficiency. Crucially, this stability was confirmed by the maintenance of the crystalline phase (Fig. 7) and the chemical integrity of the active sites, demonstrating that the UiO-66(Zr)–$(COOH)_2$ and MIL-101(Cr)–SO_3H catalysts are highly robust against deactivation under these challenging solvent-free conditions. Therefore, UiO-66(Zr) and MIL-101(Cr) structures with functional groups such as carboxylic groups as well as sulfonic groups are considered potentially attractive heterogeneous acid catalysts to be tested in other glycerol valorisation reactions. Furthermore, the acidity of the catalyst was analysed by potential titration after catalytic use, resulting in a decrease of acidity of approximately 20% and 15% for the UiO-66(Zr)–$(COOH)_2$ and MIL-101-SO_3H, respectively.

3.6. Comparison with the literature

Upon considering the previously published works reporting the use of MOF structures for the acetalization of glycerol with acetone to produce solketal, it was possible to find few publications, and most of these used a UiO-66-based MOF structure. The first publication is from 2017, by Timofeeva *et al.*, and investigated the catalytic performance of various isostructural MOF structures, based on MIL-100(M), MIL-53(M) (M = V, Al, Fe and Cr) and mixed MIL-53(Al, V).[54] Of these, the most active catalyst was MIL-100(V), achieving 85% conversion and 97% selectivity for solketal, after approximately 1 h of reaction at room temperature, using acetonitrile as a solvent. Two years later, Bakuru *et al.* presented the first publication reporting the use of UiO-66 based MOFs as catalysts for glycerol acetalization with acetone.[42] Here, different metallic centres of UiO-66(Zr, Ce and Hf) were used. UiO-66(Hf) was shown to be the most active, achieving 97% conversion after 1 h at room temperature. Later in 2022, UiO-66 was once again reported as a catalyst for the same reaction, using this time the sulfated functionalized UiO-66(Zr) MOF structure. This acidic heterogeneous catalyst achieved a conversion of glycerol of 70% with 99.8% selectivity toward solketal at 60 °C, after 1 h.[55] More recently, in 2025, UiO-66 was used as a catalyst for solketal production, this time using

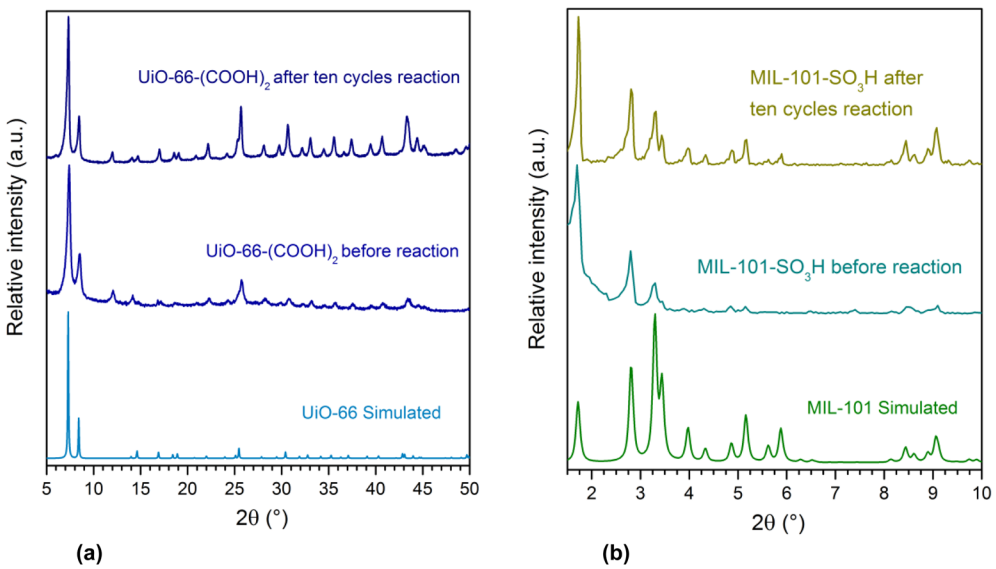

Fig. 7 XRD patterns of the UiO-66(Zr)–$(COOH)_2$ (a) and MIL-101(Cr)–SO_3H (b) catalysts after ten reaction cycles.

© 2026 The Author(s). Published by the Royal Society of Chemistry

Open Access Article. Published on 10 February 2026. Downloaded on 2/16/2026 9:47:31 AM. This article is licensed under a Creative Commons Attribution-NonCommercial 3.0 Unported Licence.

Table 4 Comparison of functionalized MOFs with high-density heterogeneous acid catalysts for glycerol acetalization

Material	Conditions	Conv. (%)	Acid density[a] (mmol H^+ per g)	Ref.
80LS20PS450H^+ (macro/mesoporous solid protonic acids)	5 wt%, 1 : 6 (gly./acet.), 60 °C, 300 rpm, 2 h	90	3.49	58
GC-1 : 2 (carbon)	3 wt%, 1 : 4 (gly./acet.), RT, 4 h	95	3.5	59
HSC-SO_3H (spherical carbon)	50 mg, 1 : 1 (gly./acet.), 80 °C, 6 h	79.1	1.9	60
PVA40 (poly(vinyl alcohol))	200 mg, 1 : 6 (gly./acet.), 70 °C, 6 h	90	4.0	61
PSF/K-SiO_2 (modified SiO_2 supported *p*-phenolsulfonic acid)	50 mg, 1 : 1 (gly./acet.), 25 °C, 1.5 h	86.3	2.6	62
UiO-66(Zr)–$(COOH)_2$	4 wt%, 1 : 6 (gly./acet.), 60 °C, 1 h	85.1	0.84	This work
MIL-101(Cr)–SO_3H	4 wt%, 1 : 6 (gly./acet.), 60 °C, 1 h	87.6	0.93	This work

[a] Total acidity based on titration.

a defective sulfated functionalized UiO-66(Zr). 79.6% glycerol conversion was obtained, with a solketal selectivity of 99.5%, after 1.5 h at 60 °C, and this catalytic activity was maintained for 5 consecutive cycles.[56] In addition to these findings, MOF-808 structures have been identified as highly promising candidates. Specifically, MOF-808(Hf) has demonstrated superior performance compared to its Zr counterpart, achieving 91% conversion after 3 h at 60 °C. This high activity, attributed to a greater density of acid centres, has been accompanied by remarkable stability, with the catalyst maintaining its performance over ten consecutive cycles without regeneration.[57]

To provide a definitive contextual analysis of the performance of the catalysts, catalyst activities were benchmarked against literature on metal–organic frameworks (MOFs) and selected high-performing heterogeneous acid catalysts, as summarised in Table 4. The novelty of this work is hereby reaffirmed: it represents the first application of MIL-101 structures for solketal synthesis *via* glycerol acetalization, and the first report of UiO-66-$(COOH)_2$ functionalization for this specific reaction. When evaluated in comparison to extant literature on the subject, MOFs, our most effective catalysts, MIL-101(Cr)–SO_3H (87.6% conversion) and UiO-66(Zr)–$(COOH)_2$ (85.1% conversion), demonstrate a high level of competitiveness under conditions that are identical and solvent-free at 60 °C. Notably, the activity of the aforementioned compounds is sustained over ten consecutive recycling cycles. This level of stability is rarely demonstrated for high-performance MOFs in this reaction.

The principal scientific advantage of the MOF approach lies in the trade-off between synthetic complexity and long-term viability. As shown in Table 4, many highly active heterogeneous catalysts (*e.g.* GC-1 : 2 and PVA40) often rely on extremely high acid site densities (up to 4.0 mmol H^+ per g) to achieve high conversions, frequently requiring complex multi-step synthetic routes, high temperatures, or extensive post-synthetic modifications. In stark contrast, the MOF architecture allows the successful integration of high concentrations of functional Brønsted acid groups, such as the sulfonic group in MIL-101(Cr)–SO_3H (0.93 mmol H^+ per g), in a single, high-yield step. This rational design provides a superior balance of high activity, synthetic economy, and exceptional robustness, validating the use of these MOFs as highly promising and sustainable heterogeneous acid catalysts for biomass valorisation.

4. Conclusions

MIL-101(Cr) and UiO-66(Zr) MOFs were prepared and functionalized with carboxylic and sulfonic groups. The characterization techniques employed allowed the confirmation of the correct preparation of the desired MOF crystalline phases and their successful functionalization. This study systematically investigated the influence of framework topology and Brønsted acid functionality on the solvent-free acetalization of glycerol, successfully synthesizing and characterizing functionalized UiO-66(Zr) and MIL-101(Cr) MOFs. The catalytic outcome proved to be highly dependent on the balance between acid site strength, concentration, and accessibility.

Within the mesoporous family, the MIL-101(Cr)–SO_3H material achieved superior catalytic performance (>85% conversion and >98% selectivity), benefiting from an optimal combination of high acid site loading and the absence of significant diffusion limitations provided by its large-pore structure. Conversely, for the microporous UiO-66(Zr) structure, the activity of the –SO_3H derivative was strongly hindered by pore constriction. Here, the UiO-66(Zr)–$(COOH)_2$ proved more effective, demonstrating that the stronger intrinsic acidity of the carboxylic groups successfully compensated for mass transfer limitations imposed by the narrower pores.

The comparative evaluation of these two distinct topologies—including the first reported use of acidic MIL-101(Cr) for solketal synthesis—establishes a crucial structure–property correlation. Our findings underscore that UiO-66(Zr)–$(COOH)_2$ and MIL-101(Cr)–SO_3H are highly effective heterogeneous catalysts, both exhibiting exceptional structural stability over ten consecutive reuse cycles. These results provide direct, rational design guidelines, highlighting that optimal catalytic efficiency for viscous substrates requires a balance of high acid strength/density with favourable textural accessibility.

Author contributions

Fátima Mirante: investigation, formal analysis, writing-original draft. Pedro Leo: conceptualization, methodology, formal

Open Access Article. Published on 10 February 2026. Downloaded on 2/16/2026 9:47:31 AM. This article is licensed under a Creative Commons Attribution-NonCommercial 3.0 Unported Licence.

analysis, writing-original draft, writing-review & editing. Carlos Palomino: methodology, investigation, formal analysis, writing-original draft. Carlos M. Granadeiro: supervision, formal analysis, writing-original draft. Luis Cunha-Silva: investigation, formal analysis, writing-review & editing, supervision. Salete Balula: writing-review & editing, supervision, resources, project administration, funding acquisition.

Conflicts of interest

There are no conflicts to declare.

Data availability

Data for this article can be found *via* the link: https://www.dropbox.com/scl/fo/zyj3tt286r9wymwucgnl4/AFozWeDx41FrTT2ChoGGn28?rlkey=znvakryabjbb9cf02r1td86bx&st=zop2rejs&dl=0. Using this link it is possible to find the manuscript, all the characterization data for the 4 different materials prepared in this work, using the different techniques performed (FTIR, XRD, SEM, *etc.*), and all the catalysis results obtained by GC for testing the catalytic efficiency of the different acidic materials.

Supplementary information (SI) is available. See DOI: https://doi.org/10.1039/d5ra07900d.

Acknowledgements

This work received financial support from the PT national funds (FCT/MECI, Fundação para a Ciência e Tecnologia and Ministério da Educação, Ciência e Inovação) through the project UID/50006-Laboratório Associado para a Química Verde – Tecnologias e Processos Limpos. FCT/MECI is also acknowledged for funding through the Individual Call to Scientific Employment Stimulus with the references CEECIND/09076/2023 (FM), 2022.02651.CEECIND/CP1724/CT0011 (CMG), CEECIND/00793/2018 (LCS) and CEECIND/03877/2018 (SSB). PL gratefully acknowledge the financial support of Universidad Rey Juan Carlos for IMPULSO Project (Grant M-3729).

References

1 M. Tomatis, H. K. Jeswani and A. Azapagic, *Waste Manage.*, 2024, **179**, 55–65.
2 Y. Gu and F. Jérôme, *Green Chem.*, 2010, 1127–1138.
3 A. A. Smirnov, S. A. Selishcheva and V. A. Yakovlev, *Catalysts*, 2018, **8**, 1–25.
4 V. Domínguez-Barroso, C. Herrera, M. A. Larrubia, R. González-GIl, M. Cortés-Reyes and L. J. Alemany, *Catalysts*, 2019, **9**, 609–622.
5 K. Archana, N. G. Pillai, K. Y. Rhee and A. Asif, *Composites, Part B*, 2019, **158**, 384–389.
6 A. L. Olson, M. Tunér and S. Verhelst, *Heliyon*, 2023, **9**, e13041.
7 B. Malakar, S. Bhattacharjee, N. Q. M. Tran, T. Le Hoang Doan, T. B. Phan, S. Chongdar and A. Bhaumik, *Chem. Commun.*, 2024, **61**, 81–84.
8 S. Ammaji, G. S. Rao and K. V. R. Chary, *Appl. Petrochem. Res.*, 2018, **8**, 107–118.
9 J. K. A. Held, *React. Kinet., Mech. Catal.*, 2016, **117**, 341–352.
10 R. Zhou, Y. Jiang, H. Zhao, B. Ye, L. Wang and Z. Hou, *Fuel*, 2021, **291**, 120207.
11 R. Zhou, B. Ye and Z. Hou, *Fuel*, 2023, **354**, 129325.
12 Y. Jiang, X. Li, H. Zhao and Z. Hou, *Fuel*, 2019, **255**, 115842.
13 S. Gadamsetti, N. P. Rajan, G. S. Rao and K. V. R. Chary, *J. Mol. Catal. A:Chem.*, 2015, **410**, 49–57.
14 F. Coccia, N. D'Alessandro, A. Mascitti, E. Colacino and L. Tonucci, *ChemCatChem*, 2024, **16**, 202301672.
15 A. Kirchon, L. Feng, H. F. Drake, E. A. Joseph and H.-C. Zhou, *Chem. Soc. Rev.*, 2018, **47**, 8611–8638.
16 D. Li, A. Yadav, H. Zhou, K. Roy, P. Thanasekaran and C. Lee, *Glob. Chall.*, 2024, **8**, 2300244.
17 F. zohra Zeggai, Z. Ait-Touchente, K. Bachari and A. Elaissari, *Chem. Phys. Impact*, 2025, **10**, 100864.
18 X. Kong, H. Deng, F. Yan, J. Kim, J. A. Swisher, B. Smit, O. M. Yaghi and J. A. Reimer, *Science*, 2013, **341**, 882–885.
19 D. K. Yoo, G. Lee, M. M. H. Mondol, H. J. Lee, C. M. Kim and S. H. Jhung, *Coord. Chem. Rev.*, 2023, **474**, 214868.
20 X.-J. Kong and J.-R. Li, *Engineering*, 2021, **7**, 1115–1139.
21 J. F. Blandez, A. Santiago-Portillo, S. Navalón, M. Giménez-Marqués, M. Álvaro, P. Horcajada and H. García, *J. Mol. Catal. A:Chem.*, 2016, **425**, 332–339.
22 A. Dhakshinamoorthy, Z. Li and H. Garcia, *Chem. Soc. Rev.*, 2018, **47**, 8134–8172.
23 J. Guo, Y. Qin, Y. Zhu, X. Zhang, C. Long, M. Zhao and Z. Tang, *Chem. Soc. Rev.*, 2021, **50**, 5366–5396.
24 A. Dhakshinamoorthy, A. Santiago-Portillo, A. M. Asiri and H. Garcia, *ChemCatChem*, 2019, **11**, 899–923.
25 P. L. Llewellyn, S. Bourrelly, C. Serre, A. Vimont, M. Daturi, L. Hamon, G. De Weireld, J.-S. Chang, D.-Y. Hong, Y. Kyu Hwang, S. Hwa Jhung and G. Férey, *Langmuir*, 2008, **24**, 7245–7250.
26 J. Sun, G. Yu, Q. Huo, Q. Kan and J. Guan, *RSC Adv.*, 2014, **4**, 38048–38054.
27 P. Niu, N. Lu, J. Liu, H. Jia, F. Zhou, B. Fan and R. Li, *Microporous Mesoporous Mater.*, 2019, **281**, 92–100.
28 F. Ragon, B. Campo, Q. Yang, C. Martineau, A. D. Wiersum, A. Lago, V. Guillerm, C. Hemsley, J. F. Eubank, M. Vishnuvarthan, F. Taulelle, P. Horcajada, A. Vimont, P. L. Llewellyn, M. Daturi, S. Devautour-Vinot, G. Maurin, C. Serre, T. Devic and G. Clet, *J. Mater. Chem. A*, 2015, **3**, 3294–3309.
29 P. Leo, N. Crespí, C. Palomino, A. Martín, G. Orcajo, G. Calleja and F. Martinez, *Catal. Today*, 2022, **390–391**, 258–264.
30 G. Férey, C. Mellot-Draznieks, C. Serre, F. Millange, J. Dutour, S. Surblé and I. Margiolaki, *Science*, 2005, **309**, 2040–2042.
31 J.-M. Yang, R.-Z. Zhang and Y.-Y. Liu, *CrystEngComm*, 2019, **21**, 5824–5833.
32 G. Akiyama, R. Matsuda, H. Sato, M. Takata and S. Kitagawa, *Adv. Mater.*, 2011, **23**, 3294–3297.
33 S. Brunauer, P. H. Emmett and E. Teller, *J. Am. Chem. Soc.*, 1938, **60**, 309–319.

© 2026 The Author(s). Published by the Royal Society of Chemistry

Open Access Article. Published on 10 February 2026. Downloaded on 2/16/2026 9:47:31 AM. This article is licensed under a Creative Commons Attribution-NonCommercial 3.0 Unported Licence.

34 J. Jagiello and M. Thommes, *Carbon*, 2004, **42**, 1227–1232.
35 A. F. Peixoto, M. M. A. Soliman, T. V. Pinto, S. M. Silva, P. Costa, E. C. B. A. Alegria and C. Freire, *Biomass Bioenergy*, 2021, **145**, 105936.
36 Q. Yang, V. Guillerm, F. Ragon, A. D. Wiersum, P. L. Llewellyn, C. Zhong, T. Devic, C. Serre and G. Maurin, *Chem. Commun.*, 2012, **48**, 9831.
37 B. Liu, Y. Peng and Q. Chen, *Energy Fuels*, 2016, **30**, 5593–5600.
38 F. Ragon, B. Campo, Q. Yang, C. Martineau, A. D. Wiersum, A. Lago, V. Guillerm, C. Hemsley, J. F. Eubank, M. Vishnuvarthan, F. Taulelle, P. Horcajada, A. Vimont, P. L. Llewellyn, M. Daturi, S. Devautour-Vinot, G. Maurin, C. Serre, T. Devic and G. Clet, *J. Mater. Chem. A*, 2015, **3**, 3294–3309.
39 F. M. Amombo Noa, M. Abrahamsson, E. Ahlberg, O. Cheung, C. R. Göb, C. J. McKenzie and L. Öhrström, *Chem*, 2021, **7**, 2491–2512.
40 O. I. Lebedev, F. Millange, C. Serre, G. Van Tendeloo and G. Férey, *Chem. Mater.*, 2005, **17**, 6525–6527.
41 D. Julião, F. Mirante and S. S. Balula, *Molecules*, 2022, **27**, 6573.
42 V. R. Bakuru, S. R. Churipard, S. P. Maradur and S. B. Kalidindi, *Dalton Trans.*, 2019, **48**, 843–847.
43 I. C. M. S. Santos-Vieira, R. F. Mendes, F. A. Almeida Paz, J. Rocha and M. M. Q. Simões, *Catal. Today*, 2023, **424**, 114296.
44 P. A. Oliveira, R. O. M. A. Souza and C. J. A. Mota, *J. Braz. Chem. Soc.*, 2016, **27**, 1832–1837.
45 M. R. Nanda, Z. Yuan, W. Qin, H. S. Ghaziaskar, M.-A. Poirier and C. Xu, *Appl. Energy*, 2014, **123**, 75–81.
46 M. R. Nanda, Z. Yuan, W. Qin, H. S. Ghaziaskar, M.-A. Poirier and C. C. Xu, *Fuel*, 2014, **117**, 470–477.
47 F. G. Cirujano and F. X. Llabrés i Xamena, *J. Phys. Chem. Lett.*, 2020, **11**, 4879–4890.
48 A. Talebian-Kiakalaieh, N. Aishah, S. Amin, N. Najaafi and S. Tarighi, *Front. Chem.*, 2018, **6**, 1–25.
49 S. Maurya and Y. Chandra Sharma, *RSC Adv.*, 2024, **14**, 39511–39522.
50 C. X. A. da Silva, V. L. C. Gonçalves and C. J. A. Mota, *Green Chem.*, 2009, **11**, 38–41.
51 M. S. Khayoon and B. H. Hameed, *Appl. Catal., A*, 2013, **464–465**, 191–199.
52 P. Ferreira, I. M. Fonseca, A. M. Ramos, J. Vital and J. E. Castanheiro, *Appl. Catal., B*, 2010, **98**, 94–99.
53 M. J. da Silva, A. A. Rodrigues and P. F. Pinheiro, *Fuel*, 2020, **276**, 118164.
54 M. N. Timofeeva, V. N. Panchenko, N. A. Khan, Z. Hasan, I. P. Prosvirin, S. V. Tsybulya and S. H. Jhung, *Appl. Catal., A*, 2017, **529**, 167–174.
55 Y. Jiang, R. Zhou, B. Ye and Z. Hou, *J. Ind. Eng. Chem.*, 2022, **110**, 357–366.
56 W. Wang and H. Gong, *Polyhedron*, 2025, **269**, 117407.
57 F. Mirante, P. Leo, C. N. Dias, L. Cunha-Silva and S. S. Balula, *Materials*, 2023, **16**, 7023–7034.
58 L. J. Konwar, A. Samikannu, P. Mäki-Arvela, D. Boström and J.-P. Mikkola, *Appl. Catal., B*, 2018, **220**, 314–323.
59 M. Gonçalves, R. Rodrigues, T. S. Galhardo and W. A. Carvalho, *Fuel*, 2016, **181**, 46–54.
60 L. Wang, J. Zhang, S. Yang, Q. Sun, L. Zhu, Q. Wu, H. Zhang, X. Meng and F.-S. Xiao, *J. Mater. Chem. A*, 2013, **1**, 9422.
61 N. F. Lopes, M. Caiado, P. Canhão and J. E. Castanheiro, *Energy Sources, Part A*, 2015, **37**, 1928–1936.
62 R. Zhou, Y. Jiang, H. Zhao, B. Ye, L. Wang and Z. Hou, *Fuel*, 2021, **291**, 120207.

© 2026 The Author(s). Published by the Royal Society of Chemistry